Julia-Maria Hübner, Wilder Carrillo-Cabrera, Raul Cardoso-Gil, Primož Koželj, Ulrich Burkhardt, Martin Etter, Lev Akselrud, Yuri Grin and Ulrich Schwarz*

High-pressure synthesis of $SmGe_3$

https://doi.org/10.1515/zkri-2020-0058
Received May 20, 2020; accepted June 11, 2020; published online August 10, 2020

Abstract: The new samarium germanide $SmGe_3$ is obtained by high-pressure high-temperature synthesis of pre-reacted mixtures of samarium and germanium at a pressure of 9.5 GPa and temperatures between 1073 and 1273 K. $SmGe_3$ decomposes at 470(5) K into $SmGe_2$, α-Sm_3Ge_5 and a hitherto unknown phase. $SmGe_3$ exhibits a superstructure of the cubic Cu_3Au-type. Transmission electron microscopy measurements of crystalline particles and prepared lamellae indicate a high density of defects on the nanoscale. Selected area electron diffraction and elaborate X-ray powder diffraction measurements consistently indicate a $2a_0 \times 2a_0 \times 2a_0$ superstructure adopting space group $Fm\bar{3}m$ with a = 8.6719(2) Å.

Keywords: Cu_3Au-type; germanium; high pressure; samarium; symmetry relationship.

Dedicated to Professor Dr. Ulrich Müller on the occasion of his 80th birthday.

1 Introduction

The elemental semiconductors silicon and germanium form a rich variety of binary phases with electropositive partners of the alkaline, alkaline-earth or rare-earth metal groups, and their chemical bonding as well as their electron count is often within the scope of the Zintl-Klemm concept [1, 2]. The tetrel atoms form one-, two- or three-dimensional partial structures with two-center two-electron bonds, frequently yielding electron-precise electron balances. The application of high-pressure techniques has proven to be a productive strategy to grant access to structural patterns that violate classical electron counting rules.

Systematic studies of tetrel connectivities in MT_3 compounds (M: alkaline earth or rare-earth metal; T: Si, Ge) [3–23] disclose a number of structural motifs that go beyond the scope of the 8-N rule. Moreover, the phases formed with diamagnetic metal ions repeatedly exhibit superconductivity with strong electron-phonon coupling. Within the set of manufactured phases, the absence of a corresponding samarium compound is striking. Earlier density functional theory calculations [24] predict an atomic arrangement with space group $P6_3/mmc$ for the compound $SmGe_3$. However, by high-pressure high-temperature synthesis, we obtain a Cu_3Au-like $SmGe_3$ phase. The finding of superstructure reflections motivated further investigations by energy dispersive X-ray spectroscopy, Transmission electron microscopy (TEM) and extensive X-ray powder diffraction experiments.

2 Experimental section

2.1 Synthesis

$SmGe_3$ was synthesized under high-pressure high-temperature conditions. All sample handling, except for high-pressure synthesis itself, was performed in argon-filled glove boxes (MBraun, H_2O and O_2 < 0.1 ppm). The precursor mixture was prepared by arc melting of samarium (Lamprecht, 99.9%) and germanium (Chempur, 99.9999+%) in the ratio 1:3 plus 6% excess of samarium for the compensation of evaporation losses during heating. The material was ground and filled into BN crucibles before being transferred into MgO octahedra with an edge length of 18 mm. High-pressure high-temperature syntheses were conducted in a Walker-type module [25] for 30 min to 5 h at pressures between 9(1) to 9.5(10) GPa and temperatures from 1073(107) and 1273(127) K before quenching under load. The calibration of pressure and temperature has been realized prior to the experiments by the observation of resistance changes of bismuth [26] and thermocouple-calibrated runs, respectively.

2.2 Sample characterization

For metallographic analysis, samples were prepared by polishing with diamond powder disks (grain size 6, 3 and 0.25 µm) after embedding in paraffin. The investigation was realized with a Philips XL 30 scanning electron microscope (SEM) (LaB_6 cathode), comprising an EDAX Si(Li) detector for energy-dispersive X-ray spectroscopy (EDXS).

***Corresponding author: Ulrich Schwarz**, Max-Planck-Institut für Chemische Physik fester Stoffe, Nöthnitzer Straße 40, 01187 Dresden, Germany, E-mail: Ulrich.Schwarz@cpfs.mpg.de
Julia-Maria Hübner, Wilder Carrillo-Cabrera, Raul Cardoso-Gil, Primož Koželj, Ulrich Burkhardt, Lev Akselrud and Yuri Grin: Max-Planck-Institut für Chemische Physik fester Stoffe, Nöthnitzer Straße 40, 01187 Dresden, Germany, E-mail: Julia.Huebner@cpfs.mpg.de (J.M. Hübner), Wilder.Carrillo-Cabrera@cpfs.mpg.de (W. Carrillo-Cabrera), Raul.Cardoso@cpfs.mpg.de (R. Cardoso-Gil), Primoz.Kozelj@cpfs.mpg.de (P. Koželj), Ulrich.Burkhardt@cpfs.mpg.de (U. Burkhardt), Lev.Akselrud@cpfs.mpg.de (L. Akselrud), Juri.Grin@cpfs.mpg.de (Y. Grin). https://orcid.org/0000-0003-2048-6629 (J.M. Hübner)
Martin Etter: Deutsches Elektronen Synchrotron, Notke Straße 85, 22607 Hamburg, Germany, E-mail: Martin.Etter@Desy.de

Differential scanning calorimetry (DSC) experiments were performed in a Netzsch DSC 404 C device (Netzsch-Gerätebau GmbH, Selb, Germany) operated with heating and cooling rates of 10 K/min under argon atmosphere using corundum crucibles.

Phase designation was conducted by X-ray powder diffraction experiments with a Huber Image Plate Guinier Camera G670 (Huber Diffraktionstechnik GmbH & Co. KG, Rimsting, Germany), using $CuK\alpha_1$ radiation (λ = 1.54056 Å). X-ray diffraction experiments for structure refinement were realized with synchrotron radiation (λ = 0.20709 Å) at DESY Group PETRA III using beamline P02.1, and with a Stoe Stadi MP in Bragg-Brentano geometry. The diffractometer was equipped with a DECTRIS MYTHEN2 1K silicon strip detector and operated with $Cu\text{-}K\alpha_1$ radiation (λ = 1.54056 Å, curved germanium (111) Johann-type Monochromator). The sample with cylindrical shape was mounted on a zero background sample holder with one of the cross sectional area at its end oriented to the incident X-ray beam. For better data point statistics, the final powder pattern results from the sum of three individual intensity data sets, collected in the angular range 5.00° ≤ 2θ ≤ 120° (scan step = 0.06°, time pro step 40 s, $t_{total} \approx$ 24 h).

All crystallographic calculations including determination of diffraction peak positions as well as lattice parameter and structure refinements on basis of full diffraction profiles (Rietveld technique) were performed with the WinCSD program package [27].

Thin samples for the TEM study were prepared by the focused-ion-beam (FIB) lift-out technique. Thin cross-sections of micro-crystalline grains were extracted from a broken bulk fragment. Defined crystallographic oriented cross-sections were prepared perpendicular to the staking-faults visible at the fracture surface. The FIB lift-out technique was performed on a FEI Quanta 200 3D ion/electron dual beam device (FEI Company, Eindhoven, the Netherlands) equipped with an Omniprobe micro-manipulator (tungsten needle), and can be used both as a SEM and a scanning ion microscope (SIM). First, protecting Pt layers (24 × 2 µm thickness, 2 µm high) were deposited on selected parts (parallel and perpendicular to the *c* axis of microcrystalline arrays) using an acceleration voltage of 30 kV and a current of 0.1 nA. Each cross section (2 µm thickness) was prepared by applying a Ga-ion beam using an acceleration voltage of 30 kV and a current of 1–0.5 nA. The manufactured cut was transferred onto a copper Omniprobe TEM holder using the in-situ lift-out technique [3]. Finally, the cross section was thinned in several discrete steps down to a thickness of about 40 nm by applying an acceleration voltage of 30 kV with currents of 0.5–0.01 nA of the Ga-ion beam.

Magnetic susceptibility was measured using a polycrystalline sample of cylindrical shape (3.0 × 2.5 × 3.4 mm) on an SQUID magnetometer (MPMS XL-7, Quantum Design) between 1.8 and 300 K in external fields of 0.01 to 3.5 T. Electrical resistivity measurements were conducted in a temperature range from 1.8 to 300 K by using the four-point probes method with a Keithley DC current source and a Hewlett Packard nanovoltmeter inside a helium flow cryostat at zero magnetic field. The contacting of the sample with Cu wire was done inside the glove box with Ag paint.

3 Results

3.1 Composition and properties

The new samarium germanide is synthesized by high-pressure high-temperature treatment of pre-reacted $Sm_{25.4}Ge_{74.6}$ mixtures. The average chemical composition of the product as determined by energy dispersive X-ray spectroscopy amounts to $Sm_{25.5(5)}Ge_{74.5(5)}$ or $SmGe_{2.92(8)}$.

Differential scanning calorimetry measurements (Figure 1) of $SmGe_3$ reveal a decomposition into $SmGe_2$ [28], Sm_2Ge_5 [29] and a hitherto unknown phase at 470(5) K. The feature at 737(5) K is attributed to a reaction of the decomposition products into $SmGe_2$ [28] and Ge [30]. In full agreement with the ambient-pressure phase diagram [31], effects at 1030(5) K and 1103(5) K correspond to the peritectoid decomposition of $SmGe_2$ into Sm_2Ge_3 and Ge as well as to the melting of the resulting eutectic, respectively.

The magnetic susceptibility χ measured in an external field of $\mu_0 H$ = 3.5 T between 1.8 and 300 K (Figure 2) indicates van Vleck-type paramagnetic behavior, denoting the influence of the external field on the wave function and the transition towards excited states. Under consideration of the slope of the experimental data, the typical minimum of χ(T) for Sm^{3+} compounds is expected to occur around 400 K. The electrical resistivity ρ at zero-field between 1.8 and 300 K (Figure 2, inset) denotes metallic behavior with a room temperature value ρ(300 K) of 122 µΩcm and an inflection, which is attributed to the reduced scattering of charge carriers in the magnetically ordered phase [32]. The ordered state is antiferromagnetic as indicated by the cusp at 23 K in χ(T).

3.2 Substructure

X-ray powder diffraction patterns of $SmGe_3$ evidence that the strongest reflections indicate a Cu_3Au-type structure

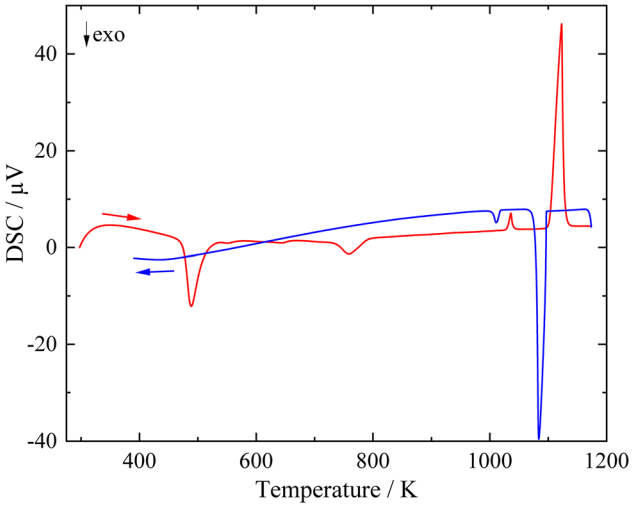

Figure 1: Differential scanning calorimetry (DSC) curve of $SmGe_3$ taken on heating (red curve) and cooling (blue curve) in the temperature range from 300 to 1175 K with a heating rate of 10 K min^{-1} at ambient pressure under argon atmosphere.

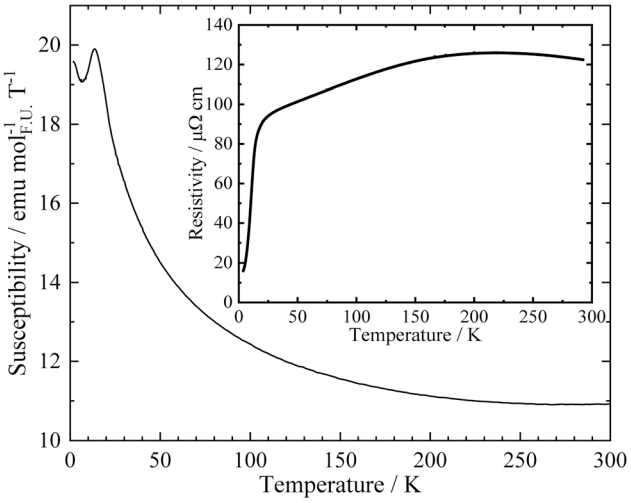

Figure 2: Magnetic susceptibility χ of $SmGe_3$ for $\mu_0 H$ = 3.5 T at temperatures between 1.8 and 300 K. Inset: Electrical resistivity of $SmGe_3$ at zero-field in the same temperature range.

motif [33]. A similar atomic arrangement is also reported for analog phases MGe_{3-x} ($x \approx 0.15$: M = Tb, Dy, Yb [34, 35]; x = 0: M = Ce [14], Np [36], Pu [37] and U [38], as well as for $SmSn_3$ [39]), the corresponding tin compound of samarium. The crystal structure represents an ordered variety of an *fcc* lattice, with germanium atoms occupying the centers of cube faces and samarium being positioned on the vertices.

The refinement of a Cu_3Au-type model using full diffraction profiles (Figure 3) results in a_0 = 4.337(3) Å with R(P) = 0.043 and wR(P) = 0.063. As some other isostructural phases exhibit germanium deficiencies, partial occupation

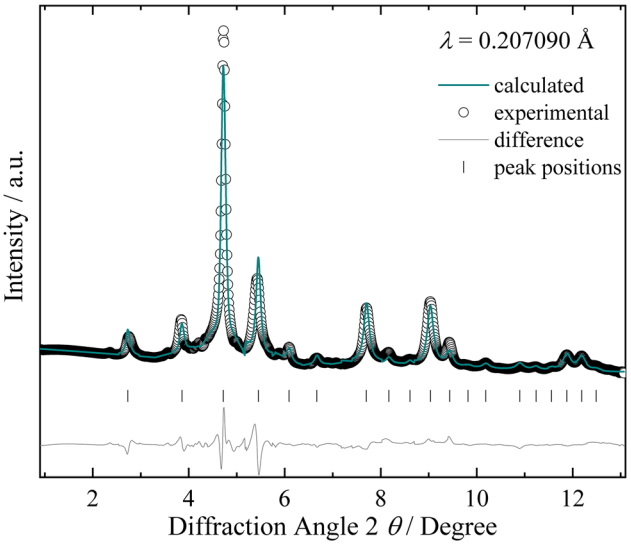

Figure 3: Synchrotron powder XRD pattern of $SmGe_{3-x}$ (see main text) and the result of refining a Cu_3Au-type substructure using full diffraction profiles (Rietveld method).

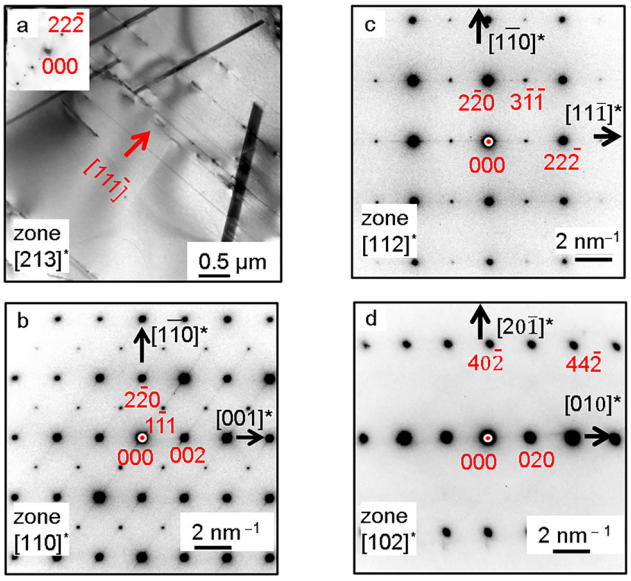

Figure 4: a) TEM image of a FIB $SmGe_3$ lamella oriented along [213] direction. The inserted [213]* Selected area (electron) diffraction (SAED) pattern is taken from an area free of {111} stacking-faults, therefore, the diffuse lines along the [111]* direction are absent. In the TEM image, the [11-1] direction is indicated by the red arrow. Dark bands are inclined {111} stacking faults; SAED diffraction images for $SmGe_3$ phase (observed in almost all the FIB lamellar area) along the zone directions, b) [110]*, c) [112]* and d) [102]*. The observed reflection conditions are in agreement with the reflection conditions for a face-centered lattice. The diffuse lines in b) and c) originate from {111} stacking-faults/twin-boundaries.

of the Ge site has been tested. The refinement proceeds without improvement of the residuals so that the models for phases $SmGe_3$ and $SmGe_{2.84(2)}$ yield R(P) = 0.0429 and wR(P) = 0.0629 in the substructure.

3.3 Superstructure

Closer inspection of the substructure refinement reveals significant extra reflections not being accounted for by the Cu_3Au-aristotype, e.g., that at 2.36°. The finding points at a larger unit cell for $SmGe_3$ and motivated additional investigations of the crystal structure. For this purpose, annealed samples (55 h at 823 K and 9.5 GPa) are selected and cleaved in order to avoid peak broadening because of grinding. Nevertheless, transmission electron microscopy investigations of a selected lamella prepared by the focused ion-beam method still reveal the presence of extended structural defects in the microstructure (Figure 4a).

SAED (Figure 4b–d) and X-ray powder diffraction patterns consistently evidence a $2a_0 \times 2a_0 \times 2a_0$ superstructure (a_0 unit cell of the primitive cubic phase). Systematic absences are compatible with a face-centered

Table 1: Information on data collection, structure refinement and crystallographic information crystal structure of $SmGe_3$. CCDC 2006311 contains the supplementary crystallographic data for this paper. These data can be obtained free of charge from The Cambridge Crystallographic Data Centre via www.ccdc.cam.ac.uk/data_request/cif.

Composition	**$SmGe_3$**
Space group, Pearson symbol, Structure type	$Fm\bar{3}m$, $cF32$, $SmGe_3$
Lattice parameters (with ABCR LaB_6)	
a/Å	8.6719(2)
V/Å^3	652.14(4)
Formula units, Z	4
Density/g cm^{-3}	7.49(1)
Measurement range	$5.015 \le 2\theta \le 120.005$
	$0 \le h \le 5$, $0 \le k \le 6$, $1 \le l \le 9$
Measd points/reflections	7667/40
R(P)/wR(P)	0.0211/0.0363

Table 2: Atom type, Wyckoff position, site occupancy factor (S.O.F.), relative atomic coordinates x, y, z, isotropic displacement parameter B_{iso} and site occupancy factors for the crystal structure of $SmGe_3$.

Atom	**Site**	***x*/*a***	***y*/*b***	***z*/*c***	**B_{iso}**	**S.O.F.**
Sm	8*c*	¼	¼	¼	0.27(1)	1.0
Ge	24*e*	0.2366(2)	0	0	0.63(1)	1.0

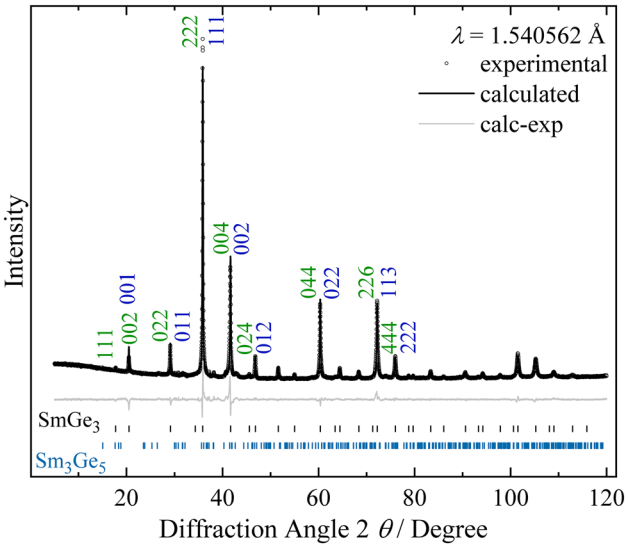

Figure 5: X-ray powder diffraction diagram of $SmGe_3$ measured in reflection alignment. Blue indices refer to the Cu_3Au-type substructure; green ones to the $2 \times 2 \times 2$ superstructure. The tick marks below the experimental pattern and the difference curve indicate line positions for the main (black) and the side phase (ocean blue).

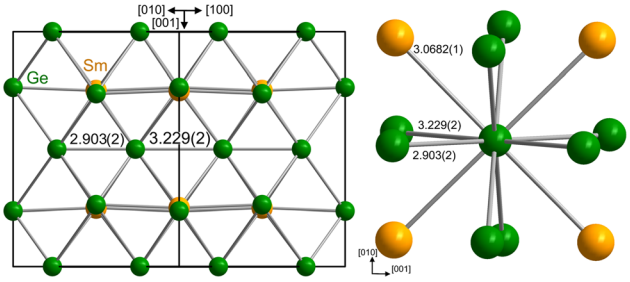

Figure 6: Crystal structure of $SmGe_3$. (left) Segment visualizing the distortion of the germanium substructure; (right) coordination sphere of the germanium atom.

lattice. As the synchrotron X-ray diffraction experiment evidences significant broadening of the diffraction profiles upon grinding of the material, subsequent X-ray measurements are performed with as-grown ingots at the cost of reduced powder average. Thus, diffraction data of several samples had to be collected in order to check for reproducibility of the intensity information. The best result has been achieved for a sample having been manufactured at 9.5 GPa by heating the starting mixture to 1273 K for 30 min before annealing at 823 K for 5 h to increase the size of the crystal domains. The corresponding diffraction patterns evidence a number of weak reflections, which are absent in the non-annealed samples. In order to test if the extra lines have to be attributed to (potentially incommensurate) modulations of the superstructure, metallographic investigations have been performed. The measurements reveal the presence of a small amount of a side product with composition Sm:Ge ≈ 1:2. As the diffraction peak positions of the previously reported compounds with similar composition do not match the extra lines, a reference sample was synthesized at the same conditions as the 1:3 phase. The X-ray powder diffraction diagram of this component is compatible with a Pu_3Pd_5-type [40] crystal structure and fits the extra lines in the pattern of $SmGe_3$. With these pieces of information at hand, a model for the superstructure of $SmGe_3$ was developed in space group $Fm\bar{3}m$ and refined (Tables 1 and 2 and Figure 5). Decrease to tetragonal symmetry (sg $I4/mmm$, $a_t = \sqrt{2}\, a_0$, $c_t = 2\, a_0$) does not result in improvements of the residuals of the least squares refinements. Further details on an ordered variety with presumably monoclinic symmetry and on the Pu_3Pd_5-type phase will be reported elsewhere.

The atomic arrangement of the $2a_0 \times 2a_0 \times 2a_0$ superstructure represents a new variety of the Cu_3Au-type. The decrease of symmetry with respect to the *lt*-Cu_3Au type [33] adds a degree of freedom to the positions of the germanium atoms. While germanium is coordinated by eight germanium and four metal atoms at the same

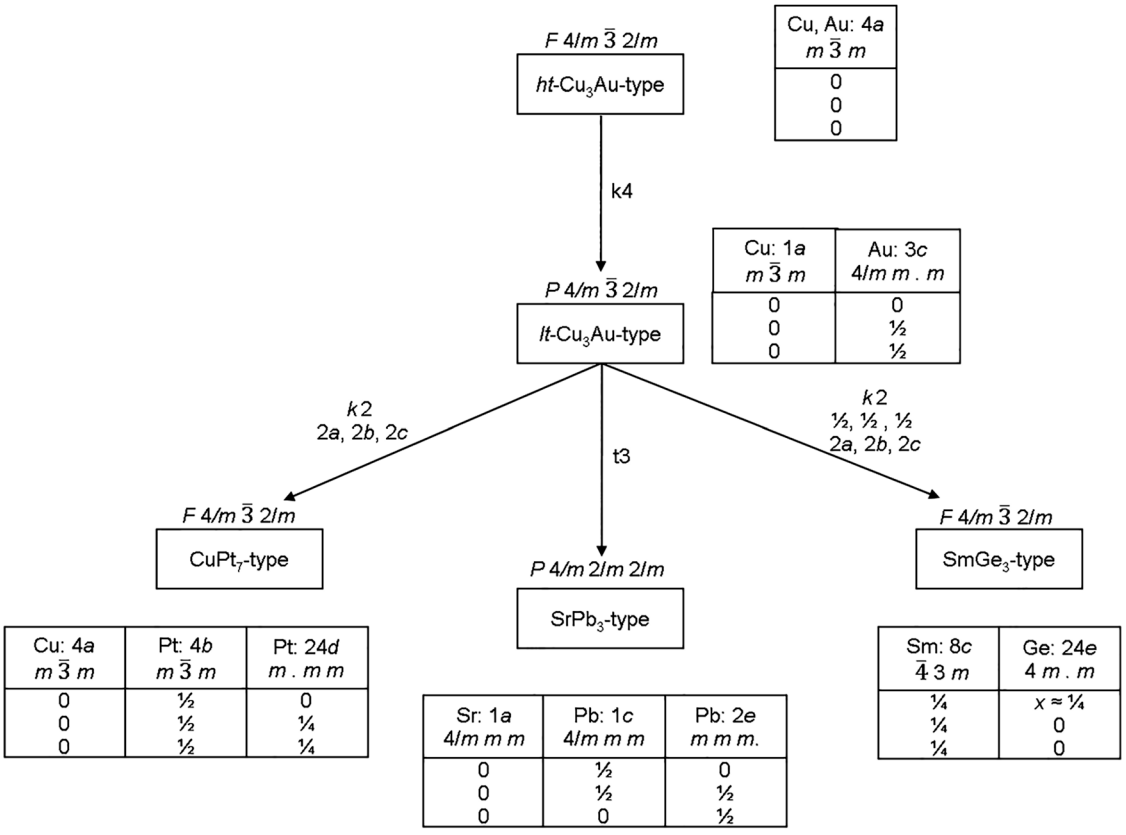

Figure 7: Group-subgroup schemes for the structures of *ht*- and *lt*-Cu_3Au [43, 33], $CuPt_7$ [44, 45], $SrPb_3$ [46] and $SmGe_3$. Indices for klassengleiche (*k*) and translationengleiche (*t*) symmetry reductions, unit cell transformations, and atomic positions are given.

distance in the undistorted *lt*-Cu_3Au arrangement (corresponding to 12 distances of $a_0/\sqrt{2}$ = 3.067(2) Å for the substructure), the distances amount to d_1(Ge–Ge) = 2.903(2) Å and d_2(Ge–Ge) = 3.229(2) Å, while the contacts *d*(Sm–Ge) = 3.0682(1) Å remain essentially unchanged in the superstructure of $SmGe_3$ (Figure 6).

The symmetry relation between the sub- and the superstructure is concisely described by a group subgroup relationship [41, 42] evidencing a klassengleiche transition of order 2. The relationship considering also some other *fcc* varieties is summarized in form of a small family tree (Figure 7) and the atomic arrangements are shown (Figure 8).

Within the series of rare earth metal trigermanides MGe_3 (*M* = La, Ce, Eu, Gd, Tb, Dy, Ho, Er, Tm, Yb, Lu) [12–22] and their variants MGe_{3-x} (M = Tb, Dy, Yb) [34, 35] and MGe_{3+x} (*M* = Nd, Pr) [21], different structural motifs are observed. The overview (Figure 9) illustrates that the selected parameters do not allow for a clear separation, but

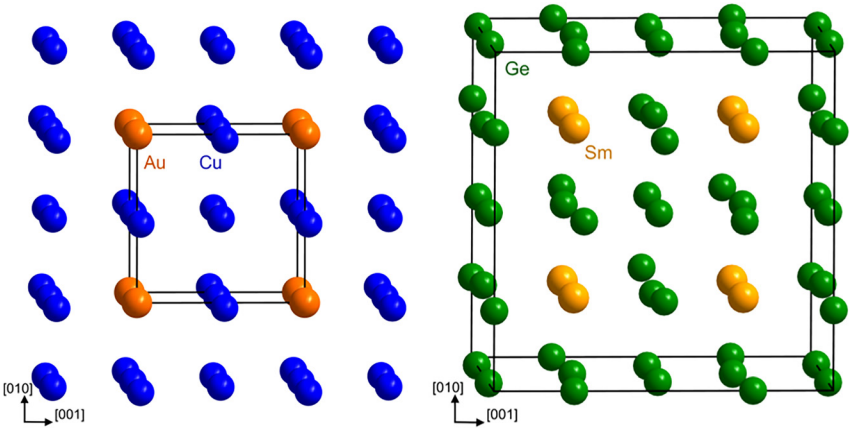

Figure 8: Segments of the crystal structures of (left) *lt*-Cu_3Au [33] and (right) the $2 \times 2 \times 2$ superstructure of $SmGe_3$. The unit cells are indicated by black lines. The atomic arrangement of $SrPb_3$ [46] corresponds to that of *lt*-Cu_3Au with a subtle tetragonal distortion (c/a = 1.014).

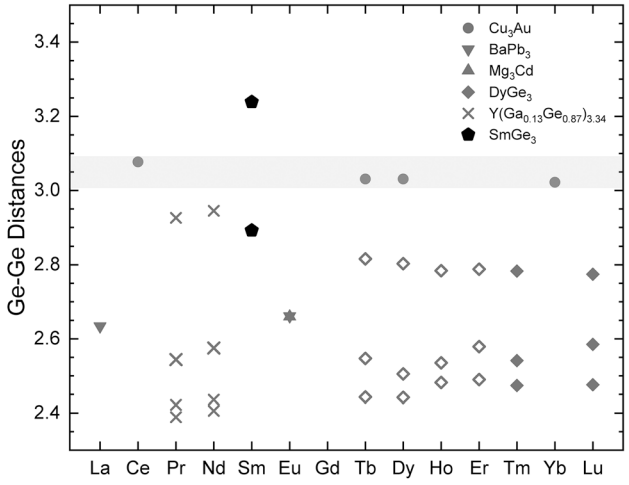

Figure 9: Average interatomic distances *d*(Ge–Ge) of selected compounds MGe_3 (*M* = La; rare-earth metal except Pm) [12–22, 35]. Only bond distances resulting from crystal structure refinements (except *lt*-Cu_3Au) are considered. Filled symbols denote compounds synthesized by high-pressure methods, empty ones phases synthesized at ambient pressure. The grey field indicates distances *d*(Ge–Ge) of compounds being assigned to the *lt*-Cu_3Au type. References to the crystal structures are given in form of structure types.

a general tendency comes to light. The extended stability field of the $DyGe_3$ type includes the heavier rare-earth metal trigermanides (*M* = Tb, Dy, Ho, Er; Tm and Lu, but except Yb). The compounds of the lighter rare-earth metals among these form at ambient pressure, only the Tm and Lu compound require high-pressure synthesis. Light rare-earth metals (*M* = Ce, Tb, Dy; but also Yb) form dense-packed *lt*-Cu_3Au-type arrangements at elevated pressures.

The interatomic distances *d*(Ge–Ge) of all structure types except Cu_3Au fall into the range from 2.4 to roughly 3 Å (Figure 9). Within the series of isotypic $DyGe_3$-type compounds, the distances *d*(Ge–Ge) remain more or less constant (distances *d*(*M*–Ge) decrease with increasing atomic number in accordance with the lanthanide contraction, not shown). Compounds, which are reported to adopt the lt-Cu_3Au-type structure, exhibit unusually long interatomic distances *d*(Ge–Ge). This abnormality is attenuated by the symmetry breaking in the new $SmGe_3$-type arrangement. The distortion induces a subdivision of the Ge–Ge distances into two groups. The shorter contacts, representing half of the distances *d*(Ge–Ge), fall now into the upper part of the range observed for $DyGe_3$-type compounds and phases $REGe_{3+x}$ (*RE* = Pr, Nd). Whether the underlying reason for the distortion is the formation of Ge–Ge bonds or the stereochemical activity of lone pairs located at the Ge^- species (assuming the electron balance $Sm^{3+}[Ge^-]_3$) will be the topic of future investigations by quantum chemical methods.

Author contribution: All the authors have accepted responsibility for the entire content of this submitted manuscript and approved submission

Research funding: Funded by International Max Planck Research School for Chemistry and Physics of Quantum Materials (IMPRS-CPQM).

Conflict of interest statement: The authors declare no conflicts of interest regarding this article.

References

1. Zintl E., Brauer G. Z. *Phys. Chem. B* 1933, *20*, 245.
2. Zintl E. *Angew. Chem.* 1939, *52*, 1.
3. Schwarz U., Wosylus A., Rosner H., Schnelle W., Ormeci A., Meier K., Baranov A., Nicklas M., Leipe S., Müller C. J., Grin Yu. *J. Am. Chem. Soc.* 2012, *134*, 13558.
4. Hübner J.-M., Akselrud L., Schnelle W., Burkhardt U., Bobnar M., Prots Yu., Grin Yu., Schwarz U. *Materials* 2019, *12*, 145.
5. Meier K., Cardoso-Gil R., Schwarz U. *Z. Kristallogr. NCS* 2011, *226*, 297.
6. Wosylus A., Prots Yu., Schwarz U. *Z. Kristallogr. NCS* 2011, *226*, 295.
7. Schnelle W., Ormeci A., Wosylus A., Meier K., Grin Yu., Schwarz U. *Inorg. Chem.* 2012, *51*, 5509.
8. Nishikawa T., Fukuoka H., Inumaru K. *Inorg. Chem.* 2015, *54*, 7433.
9. Castillo R., Schnelle W., Baranov A., Burkhardt U., Bobnar M., Cardoso-Gil R., Schwarz U., Grin Yu. *Z. Naturforsch. B* 2016, *71*, 585.
10. Castillo R., Baranov A., Burkhardt U., Cardoso-Gil R., Schnelle W., Bobnar M., Schwarz U. *Inorg. Chem.* 2016, *55*, 4498.
11. Fukuoka H., Tomomitsu Y., Inumaru K. *Inorg. Chem.* 2011, *50*, 6372.
12. Belyavina N. M., Markiv V. Y., Speka M. V. *J. Alloys Compd.* 1999, *283*, 162.
13. Fukuoka H., Suekuni K., Onimaru T., Inumaru K. *Inorg. Chem.* 2011, *50*, 3901.
14. Fukuoka H., Yamanaka S. *Chem. Lett.* 2004, *33*, 1334.
15. Castillo R., Baranov A., Burkhardt U., Grin Yu., Schwarz U. *Z. Anorg. Allg. Chem.* 2015, *641*, 355.
16. Savysyuk I. A., Gladyshevskii E. I., Gladyshevskii R. E. In: *Proceedings of the 7th International Conference on Crystal Chemistry Intermetallic Compounds*, Lviv, Ukraine, 25–28 September 1999; pp. PB17.
17. Schobinger-Papamantellos P., Rodriguez Carvajal J., Buschow K. H. J. *J. Phys. Condens. Matter* 2007, *19*, 236201.
18. Schobinger-Papamantellos P., de Mooij D. B., Buschow K. H. J. *J. Alloys Compd.* 1992, *183*, 181.
19. Schobinger-Papamantellos P., Rodriguez Carvajal J., Tung L. D., Ritter C., Buschow K. H. J. *J. Phys. Condens. Matter* 2008, *20*, 195201.
20. Eremenko V. N., Obushenko I. M. *Sov. Non-Ferrous Met. Res.* 1981, *9*, 216.
21. Fukuoka H., Yoshikawa M., Baba K., Yamanaka S. *Bull. Chem. Soc. Jpn.* 2010, *83*, 323.
22. Harada M., Fukuoka H., Matsumura D., Inumaru K. *J. Phys. Chem. C* 2012, *116*, 2153.
23. Hübner J.-M., Bobnar M., Akselrud L., Prots Yu., Grin Yu., Schwarz U. *Inorg. Chem.* 2018, *57*, 10295.

24. Persson K. *Materials data on SmGe3 (SG:194) by materials project by LBNL materials project*; Berkeley, CA (United States): Lawrence Berkeley National Laboratory (LBNL); 2016, https://doi.org/10.17188/1316073.
25. Walker D., Carpenter M. A., Hitch C. M. *Am. Mineral* 1990, *75*, 1020.
26. Young D. A. *Phase diagrams of the elements*; Berkeley, CA, USA: UC Press, 1991.
27. Akselrud L., Grin Yu. *J. Appl. Crystallogr.* 2014, *47*, 803.
28. Mayer I., Eshdat Y. *Inorg. Chem.* 1968, *7*, 1904.
29. Tobash P. H., Lins D., Bobev S., Hur N., Thompson J. D., Sarrao J. L. *Inorg. Chem.* 2006, *45,* 7286.
30. Straumanis M. E., Aka E. Z. *J. Appl. Phys.* 1952, *23*, 330.
31. Gokhale A. B., Abbaschian G. J. In *Binary Alloy Phase Diagrams*; Massalski T. B. Ed. ASM International: Ohio, 1996.
32. Meier K., Cardoso-Gil R., Schnelle W., Rosner H., Burkhardt U., Schwarz U. *Z. Anorg. Allg. Chem.* 2010, *636*, 1466.
33. Johansson C. H., Linde J. O. *Ann. Phys.* 1925, *78*, 439.
34. Fukuoka H., Yamanaka S. *Chem. Lett.* 2004, *33*, 1334.
35. Tsvyashchenko A. V., Spasskiy A.V., Velichkov A. I., Salamatin A. V., Fomicheva L. N., Salamatin D. A., Ryasny G. K., Nikolaev A. V., Budzynski M., Sadykov R. A. *J. Alloys Compd.* 2013, *552*, 190.
36. Gal J., Hadari Z., Bauminger E. R., Nowik I., Ofer S. *Solid State Commun.* 1973, *13*, 647.
37. Coffinberry A. S., Ellinger F. H. In *Proceedings of the United Nations International Conference on the Peaceful Uses of Atomic Energy*, 1958, *8*, 138.
38. Iandelli A., Ferro R. *Ann. Chim.* 1952, *42*, 598.
39. Harris I. R., Raynor G. V. *J. Less-Common Met.* 1965, *9*, 7.
40. Cromer D. T. *Acta Crystalllogr. B* 1976, *32*, 1930.
41. Billiet Y., Aroyo M. I., Wondratschek H. Tables of maximal subgroups of the space groups. In *International tables for crystallography. A1. Symmetry relations between space groups*; Wondratschek H., Müller U. Eds. Wiley: Chichester UK, 2010.
42. Müller U. Relations between the Wyckoff positions. In *International tables for crystallography. A1. Symmetry relations between space groups*; Wondratschek H., Müller U. Eds. Wiley: Chichester, UK, 2010.
43. Owen E. A., Liu Y. H. *Philos. Mag.* 1947, *38*, 354.
44. Schneider A., Esch U. Z. *Elektrochem. Angew. Phys. Chem.* 1944, *50*, 290.
45. Pöttgen R., Z. *Anorg. Allg. Chem.* 2014, *640*, 869.
46. Zintl E., Neumayr S., Z. *Elektrochem. Angew. Phys. Chem.* 1933, *39*, 86.